Research Article

Haiyun Yao, Zhaoqing Sun, Xin Yan*, Maosheng Yang*, Lanju Liang*, Guohong Ma, Ju Gao, Tenten Li, Xiaoxian Song, Haiting Zhang, Qili Yang, Xiaofei Hu, Ziqun Wang, Zhenhua Li and Jianquan Yao

Ultrasensitive, light-induced reversible multidimensional biosensing using THz metasurfaces hybridized with patterned graphene and perovskite

https://doi.org/10.1515/nanoph-2021-0816
Received December 28, 2021; accepted January 29, 2022; published online February 11, 2022

Abstract: Biosensors based on terahertz (THz) metasurfaces have recently attracted widespread attention. However, few have been reported so far because it is a challenge to achieve ultrasensitive multidimensional detection in the THz spectrum. Here, we propose a novel THz biosensor that consists of a metasurfaces and a metal oxide semiconductor-like structure (MOSLS), which is based on patterned graphene–polyimide–perovskite. We varied the photoconductivity of the MOSLS via the electrostatic doping effect. The biosensor could detect whey protein down to a concentration limit of 6.25 ng/mL. Significant responses in frequency, phase, and transmission amplitude were all detected for different protein concentrations. The transmission value difference, frequency shift, and phase difference increased with the concentration of whey protein, clearly demonstrating multidimensional biosensing. Moreover, by applying lasers with different wavelengths, we have realized reversible biosensing in THz region for the first time. These results are very promising for applications of THz metasurfaces in the field of biosensing.

Keywords: biosensor; EIT; reversible; THz metasurfaces; whey protein.

Haiyun Yao and Zhaoqing Sun have contributed equally to this work.

***Corresponding authors: Xin Yan**, School of Information Science and Engineering, Zaozhuang University, Zaozhuang, 277160, China, E-mail: yxllj68@126.com. https://orcid.org/0000-0001-8985-0244; **Maosheng Yang**, School of Electrical and Optoelectronic Engineering, West Anhui University, Lu'an, 237000, China, E-mail: 2111803010@stmail.ujs.edu.cn; and **Lanju Liang**, School of Opto-electronic Engineering, Zaozhuang University, Zaozhuang, 277160, China, E-mail: lianglanju123@163.com (L. Liang)
Haiyun Yao, School of Information Science and Engineering, Zaozhuang University, Zaozhuang, 277160, China, E-mail: haiyun1990yao@163.com
Zhaoqing Sun, Faculty of Materials and Manufacturing, Beijing University of Technology, Beijing, 100124, China, E-mail: pierresun2011@hotmail.com
Guohong Ma, Department of Physics, Instrumental Analysis & Research Center, Shanghai University, Shanghai, 200444, China
Ju Gao, Qili Yang, Xiaofei Hu, Ziqun Wang and Zhenhua Li, School of Opto-electronic Engineering, Zaozhuang University, Zaozhuang, 277160, China
Tenten Li and Jianquan Yao, College of Precision Instruments and Opto-electronics Engineering, Tianjin University, Tianjin, 300072, China
Xiaoxian Song and Haiting Zhang, Institute of Micro-nano Optoelectronics and Terahertz Technology, Jiangsu University, Zhenjiang, 212013, China

1 Introduction

Metasurfaces have attracted extensive attention as a novel way to manipulate electromagnetic waves for diverse applications, including as modulators [1–5], absorbers [6, 7], and biosensors [8–14]. The primary mechanism is that the resonant modes of metasurfaces are susceptible to changes in their microenvironment. In particular, the absorbance linewidth of their electromagnetically induced transparency (EIT) is limited only by Drude damping. The EIT-like features of metasurfaces make them ideal for ultrasensitive biosensors [9, 13]. Because the characteristic vibrational modes of numerous macromolecules like proteins, DNA, and viruses are in the THz spectrum, THz metasurfaces are particularly desirable [9, 15].

Nevertheless, the development of metasurface-based THz biosensing systems is still in its initial stages [16–20]. Previous works focused mainly on change transmission amplitude or shift resonance frequency in metasurfaces as

the sole sensing index. However, the poor sensitivity of these materials must be improved to be useful as an actual application index. Phase difference is rarely reported as a sensing index. New materials and mechanisms combined with THz metasurfaces are needed to achieve ultrasensitive, multidimensional (frequency, amplitude, phase) detection of biological macromolecules.

Recently, graphene has attracted much interest because it presents several unique advantages: large specific surface area, tunable optoelectronic properties, and good biocompatibility [16, 19, 21–23]. Patterned graphene with well-defined architecture on the micrometer to submicrometer scale has become increasingly important because of its low-loss plasma characteristics [24–26]. The combination of patterned graphene and THz metasurfaces shows great potential for ultrasensitive biosensing [27]. However, simply combining graphene and metasurfaces is no longer sufficient to meet the needs of this field because it is not easy to achieve phase modulation with such materials.

At present, most research on phase-change materials focuses on metal halide perovskites [28, 29] (ABX_3, where A = methylamine(MA), B = Pb or Sn; and X = Cl, Br, or I). They have outstanding optoelectronic properties [30], such as excellent charge-carrier mobilities, bandgap tunability, and high photoluminescence quantum yield. Effectively combining the patterned graphene layer with a second optical material, especially ABX_3, is a new possibility for the design of THz biosensors. Such composite materials can not only enable multidimensional sensing but also achieve ultrasensitive detection.

Here, we propose a novel biosensor that integrates metal oxide semiconductor-like structures (MOSLS) based on patterned graphene–polyimide (PI)–perovskite ($MAPbI_3$) with EIT-like metasurfaces (later the biosensor will be labeled by PGPP@MS) to manipulate THz waves and realize ultra-sensitive, multidimensional sensing, as illustrated in Figure 1 [31, 32]. The PI film ensures the stability of $MAPbI_3$ under ambient conditions and provides stable support for the graphene. The proposed EIT-like metasurfaces enable the generation of two polarization-independent transparent windows at 0.63 THz and 1.16 THz, and may also enhance sensitivity.

As a proof of concept, whey protein is adhered to the patterned graphene of the proposed PGPP@MS biosensor and the THz transmission spectra are measured. By varying the photoconductivity of the MOSLS via the electrostatic doping (ED) effect [33, 34], frequency, phase, and amplitude responses for different concentrations of whey protein (CWP) are obtained. Our PGPP@MS biosensor can detect CWPs as low as 6.25 ng/mL.

Furthermore, the transmission value difference of (ΔV_T), frequency shift (Δf), and phase difference (ΔP) all increase with CWP between 6.25 ng/mL and 316 μg/mL, successfully realizing multidimensional biosensing. In addition, we have realized reversible biosensing in the THz region by illuminating the biosensor with lasers at different wavelengths. These results show great promise for applications of THz metasurfaces in the field of biosensing.

2 Materials and methods

2.1 Design of the PGPP@MS biosensor

A schematic layout and all geometric parameters of the proposed PGPP@MS biosensor are depicted in Figure 1. Figure 1(a) shows an overview of the fabrication process for the PGPP@MS biosensor, which begins with a 5 μm-thick PI film spin-coated on a 300 μm-thick quartz substrate (1.0 cm × 1.0 cm) (Figure 1(a), ①). An array of 0.2 μm-thick aluminum microstructure units is fabricated atop the PI layer via standard photolithography methods (Figure 1(a), ②). The dimensions of the unit cell are shown in the photomicrographs in Figure 1(b)–(d). It consists of external U-shaped (parallel long sides (PLS) and vertical long side (VLS)) and internal asymmetric spiral structures (ASS).

In the next step, a 0.25 μm-thick $MAPbI_3$ film is spin-coated onto the metasurfaces, covering the microstructures (Figure 1(a), ③). This film shows good compactness and uniform morphology, with large grain sizes and no pinholes, as shown by the top-view SEM image in the inset of Figure 1(e). Figure 1(e) also shows the x-ray diffraction (XRD) pattern of the perovskite film. Diffraction peaks are located at 14.3°, 20.3°, 23.8°, 24.7°, 28.7°, and 32.1°, corresponding to the (110), (112), (210), (202), (220), and (310) crystal planes, respectively. No characteristic peaks associated with PbI_2 or other redundant phases were observed.

Next, a PI film was spin-coated atop the $MAPbI_3$ layer (Figure 1(a), ④), which protects and isolates the $MAPbI_3$. A 1.0 cm × 1.0 cm graphene layer was then transferred onto the top surface of the PI film (Figure 1(a), ⑤). Finally, for patterning of the graphene, zinc was sputtered onto the uppermost layer of graphene in 5 nm-thick stripes to remove a carbon layer selectively from those areas (Figure 1(a), ⑥). The device was placed in dilute HCl solution (about 0.05 M) for 1 min to dissolve the zinc. The device was then rinsed with water and dried in air. This series of steps removes one layer of carbon, and the procedure can be repeated to remove additional carbon layers. Ultimately, a graphene layer with a striped pattern is obtained. A photomicrograph of the striped graphene is shown in Figure 1(b) and as an inset to Figure 1(f).

Raman spectroscopy was performed at 514 nm excitation to confirm the quality of the graphene (Figure 1(f)). The ratio between the G peak (~1578 cm^{-1}) and the G′ peak (~2699 cm^{-1}) intensities is about 1.28. The full width at half maximum of the G′ peak is 54 cm^{-1}. These features indicate that the graphene is of good quality [35]. The conductivity of graphene is about ~1.7×10^6 S/m (square resistance ~600 Ω).

The resonant features of the PGPP@MS sample were experimentally characterized with an 8f confocal terahertz time-domain

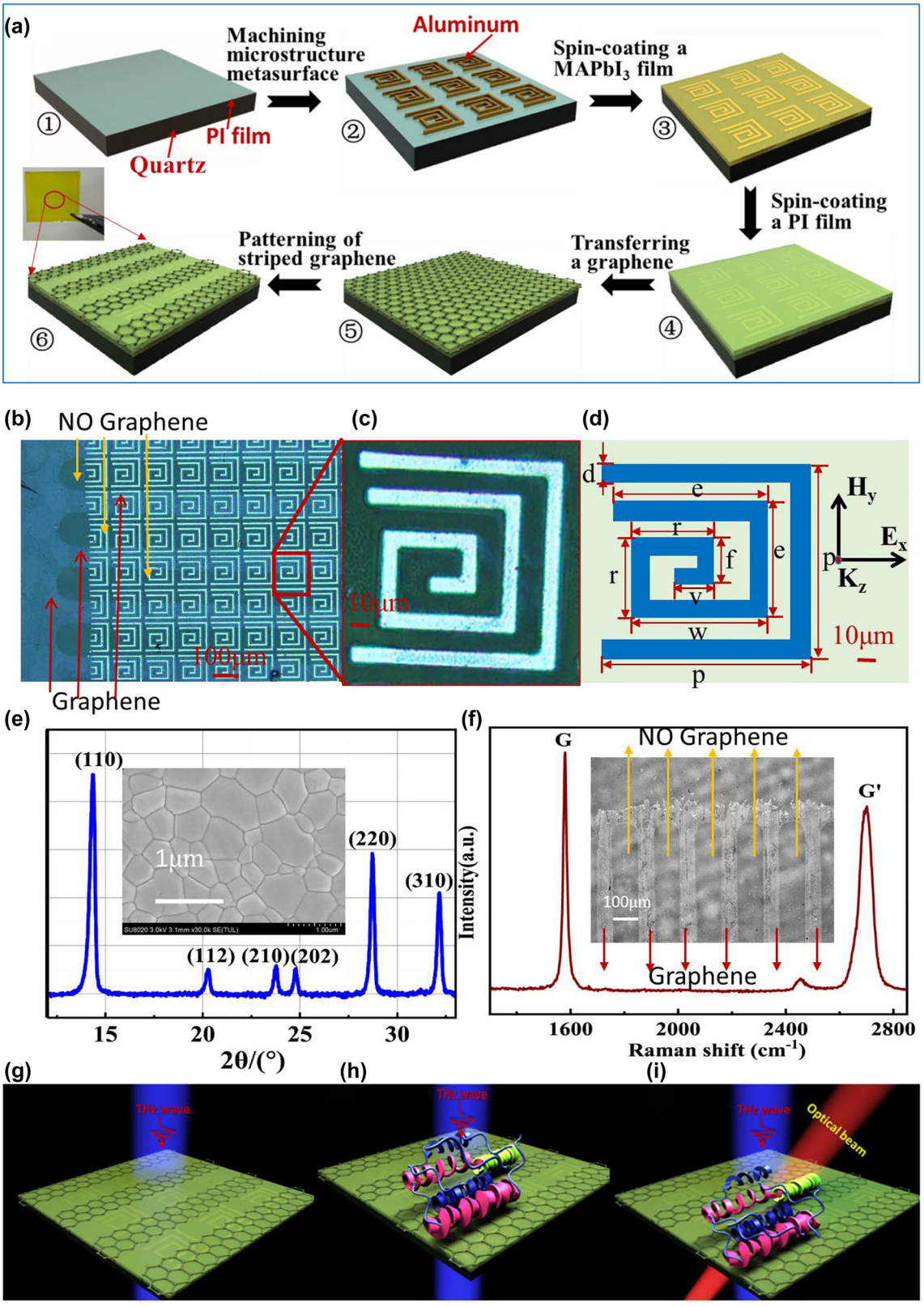

Figure 1: Fabrication and characterization of the proposed PGPP@MS biosensor.
(a) The fabrication process. ① A PI film was spin-coated on top of a quartz substrate. ② The metasurface, an asymmetric Al microstructure, was machined atop the PI film. ③ A metal halide perovskite ($MAPbI_3$) film was spin-coated on the metasurface, covering the microstructure. ④ The PI film was spin-coated onto the $MAPbI_3$ film. ⑤ A graphene layer was transferred onto the PI film. ⑥ The graphene was patterned into stripes.

spectroscopy system (see detail in Figures S1 and S2). A 405 nm/532 nm/808 nm laser with a 3 mm spot diameter was used as an optical pump (Figure 1(i)).

Whey protein was chosen as a probe analyte to verify the performance of the PGPP@MS biosensor (Figure 1(h) and (i)). We prepared five different CWP in suspension, C_1 = 6.25 ng/mL, C_2 = 2.52 µg/mL, C_3 = 46.8 µg/mL, C_4 = 316 µg/mL, and C_5 = 1.25 mg/mL. All the experimental data presented in this work are averaged after 3 tests.

2.2 Simulation of the PGPP@MS biosensor

We performed full-wave simulations with a frequency-domain solver based on finite-differential time-domain methods using CST Microwave Studio. The electric and magnetic boundary conditions were along the *x* and *y* directions (Figure 1(d)), respectively. The polarization direction of incident THz radiation was set along the *z* direction. In the simulation model, the quartz substrate was treated as a lossless dielectric with dielectric permittivity ε = 3.84 [36]. We used the classical Drude model to describe the conductivity of the graphene [37, 38]. The thickness of the graphene was set at 1 nm. The refractive index of polyimide was 3.1. The tangent loss was 0.05. The transmission $T(\omega)$ was defined as $T(\omega) = |E_s(\omega)/E_r(\omega)|^2$, where $E_s(\omega)$ and $E_r(\omega)$ are the THz electric field amplitudes of the sample and reference, respectively, after fast Fourier transformation of the THz pulses.

3 Results and discussion

3.1 Properties of the PGPP@MS biosensor

To investigate the underlying resonant mechanism of the PGPP@MS metasurfaces, the transmission spectra of the PGPP@MS biosensor were both simulated and measured,

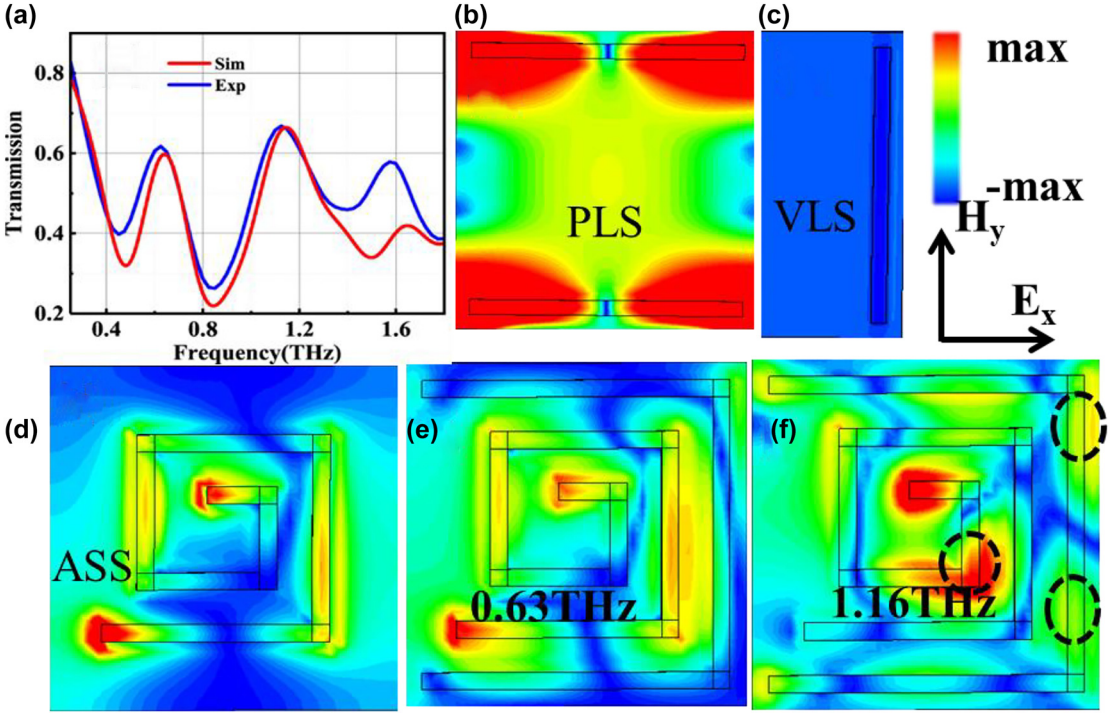

Figure 2: Simulated electric field intensity distribution of the metasurfaces: (a) experimental (blue line) and simulated (red line) transmission spectra of the PGPP@MS biosensor sample. (b)–(d) Simulated electric field intensity distributions at 0.63 THz of the PLS (b), VLS (c), and ASS (d) arrays. (e) Simulated electric field intensity distribution of the EIT mode at 0.63 THz. (f) Simulated electric field intensity distribution of the EIT mode at 1.16 THz. The dashed circles highlight field intensity that is indicative of dark mode excitation. The entire incident light is *x*-polarized.

(b) Photomicrograph of a small region of the PGPP@MS biosensor and the patterned graphene (dark blue regions indicated by red arrows). (c) Photomicrograph of a unit cell of the microstructure. (d) Schematic of the unit cell, which consists of an external U shape and an internal asymmetric spiral. The geometric parameters are, for the U shape: p = 135 µm and d = 13 µm; and for the spiral structure: e = 90 µm, w = 103 µm, r = 63 µm, f = 39 µm, and v = 31 µm. The periodicity is 150 µm. (e) X-ray diffraction (XRD) pattern for the $MAPbI_3$ film. Inset: Scanning electron microscopy (SEM) image of the $MAPbI_3$ film. (f) Raman spectrum of graphene. Inset: Photomicrograph of striped graphene. (g)–(i) Schematic illustration of the proposed biosensor. THz beams penetrate the device without whey protein at normal incidence (g). Different concentrations of protein can be deposed on the surface (h), and an external optical pump can be applied after measurement to allow reversible sensing (i).

as shown in Figure 2(a). The experimental and simulated results agree well except for a slight difference in intensity at some resonance frequencies. This deviation may have been caused by fabrication errors or differences between the simulation conditions and the actual conditions. It is also interesting to note that a transmission peak with 60% efficiency appears at around 0.63 THz and 1.16 THz, as shown in Figure 2(a). This weak transparency phenomenon reasonably suggests that there may be an EIT-like mode-coupling effect in our metasurfaces [13, 39].

To further understand the physical mechanism of the EIT-like resonances, the electric field intensities of the PLS array, VLS array, and ASS array were simulated and shown in Figure 2(b)–(d), respectively. The field is mainly distributed at the four ends of the long sides of the PLS (Figure 2(b)) and localized around the starting and ending points of the ASS (Figure 2(d)). The VLS has no electric field distribution (Figure 2(c)). Therefore, the PLS acts as the bright mode, the VLS acts as the dark mode, and the ASS acts as the quasi-dark mode, simultaneously [40]. Combining the fields of the three coupled resonators results in two transmission windows around 0.63 THz and 1.16 THz, shown in Figure 2(a).

Figure 2(e) clearly shows that the electric field intensity in the PLS is entirely suppressed at these two frequencies as a result of their destructive interference. At 0.63 THz, the field intensity is mainly localized around the starting and ending points of the ASS, indicating the excitation of the quasi-dark mode. However, at 1.16 THz, the electric field intensity is mainly concentrated around the starting point, the right corner of the ASS, and two regions on the right side (black dotted circles in Figure 2(f)), suggesting that the dark mode is now excited. Therefore, our metamaterial can produce these two EIT-like modes under *x*-polarized incident light as a result of the destructive interference of the PLS (the bright mode), the ASS (the quasi-dark mode), and the VLS (the dark mode).

3.2 Sensing performance of the PGPP@MS biosensor

To investigate the sensing performance of the PGPP@MS biosensor, whey protein at various concentrations in aqueous solution was dropped onto the surface of the device, and the experimental test was performed after the water evaporation was completed.

Concentrations of 0 ng/mL (C_0), 6.25 ng/mL (C_1), 2.52 μg/mL (C_2), 46.8 μg/mL (C_3), 316 μg/mL (C_4), and 1.25 mg/mL (C_5) were tested. The transmission spectra of the PGPP@MS biosensor covered by different CWP are shown in Figure 3(a). The overall trend of the results is that transmission value decreases with increasing CWP.

Based on the THz transmission spectra of the PGPP@MS biosensor, we chose to examine shifts in the transmission spectrum at five frequencies, f_1 = 0.42 THz, f_2 = 0.81 THz, f_3 = 1.16 THz, f_4 = 1.39 THz, and f_5 = 1.58 THz. Variations in both the frequency and the magnitude of the EIT peak occurred in the transmission spectrum as a function of CWP. At frequency points f_3, f_4, and f_5, the changes in transmission and peak frequency shifts were relatively large. In particular, ultra-sensitive detection of a very low CWP of 6.25 ng/mL was possible. We compare the sensitivity and sensing type of previous work mainly based on the interaction of external molecules with graphene (see Table 1). WP molecules have no benzene ring like structures and without π-electrons. Therefore, it cannot form π–π stacking with graphene. First, we compared the case without π–π stacking, and from Table 1, it can find that the sensitivity of our designed sensor is two orders of magnitude higher than the other two sensors. And, our biosensor realizes three-dimensional sensing. Generally, if an external molecule has a benzene ring like structure with π-electrons, it strongly interacts with the π-electrons of graphene through π–π stacking [19]. Therefore, the graphene-based sensor show higher sensitivity to the external molecules containing π-electrons [19]. However, the sensitivity of our designed sensor to detect WP molecules without π-electrons is higher than that of detecting CMM which form π–π stacking with graphene in previous work. In summary, our designed sensor has higher sensitive sensing performance.

The effect of the analyte on the behavior of the PGPP@MS biosensor can be explained by the coupled harmonic oscillator model, which describes the near-field coupling between bright- and dark-mode resonators. The coupled differential equations can analytically describe the interference [43]:

$$\ddot{x}_1 + \gamma_1\dot{x}_1 + \omega_0^2 x_1 + \kappa x_2 = E\,,$$

$$\ddot{x}_2 + \gamma_2\dot{x}_2 + (\omega_0 + \delta)^2 x_2 + \kappa x_1 = 0\,. \tag{1}$$

Here, x_1, x_2, γ_1, and γ_2 are the resonant amplitudes and losses of the bright and dark modes, respectively. ω_0 is the resonance frequency of the bright mode oscillator ($\gamma_2 \ll \gamma_1 \ll \omega_0$), δ denotes the detuning of the resonant frequency of the dark mode oscillator from the bright mode ($\delta \ll \gamma_1$), and κ is the coupling coefficient between the two oscillators. By solving Eq. (1) with the approximation $\omega - \omega_0 \ll \omega_0$, the susceptibility χ is obtained:

$$\chi = \chi_r + i\chi_i \propto \frac{(\omega + \omega_0 - \delta) + \frac{i\gamma_2}{2}}{\left(\omega - \omega_0 + \frac{i\gamma_1}{2}\right)\left(\omega - \omega_0 - \delta + \frac{i\gamma_2}{2}\right) - \frac{\kappa^2}{4}} \tag{2}$$

where χ_r is the real part of the susceptibility, and χ_i is the imaginary part, which is proportional to the energy losses.

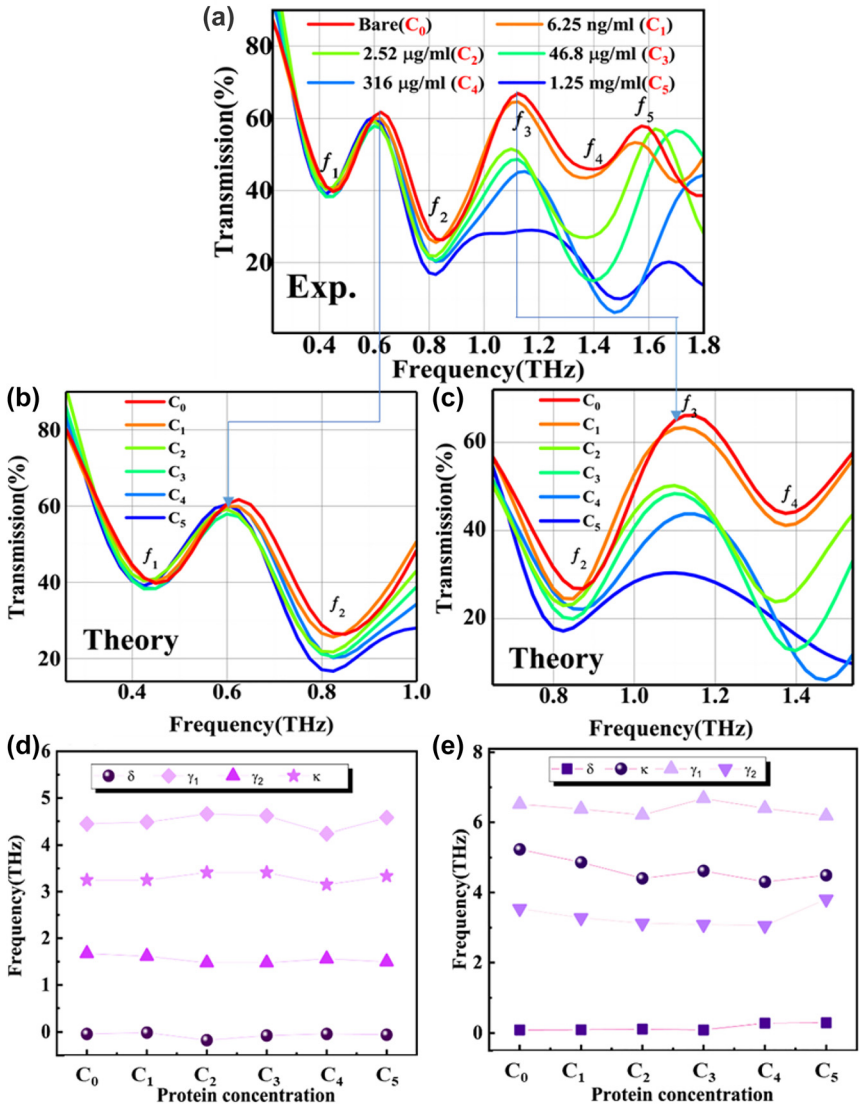

Figure 3: Experimentally measured and theoretically fitted for transmission spectra of the PGPP@MS biosensor at different CWP.
(a) Experimentally measured THz transmission spectra of the PGPP@MS biosensor at different CWP. C_0 = 0 ng/mL, C_1 = 6.25 ng/mL, C_2 = 2.52 μg/mL, C_3 = 46.8 μg/mL, C_4 = 316 μg/mL, and C_5 = 1.25 mg/mL). Peaks f_1–f_5 are indicated to illustrate the sensing effect. (b) and (c) The transmission curves obtained by theoretically fitted at each CWP for two different EIT-like frequency bands, 0.25–1.0 THz (b) and 0.62–1.58 THz (c). (d) The CWP dependence of the oscillator parameters γ_1, γ_2, δ, and κ, extracted by fitting the transmission curves in (b) with Eq. (2). (e) As in (d) for the transmission curves in (c).

Table 1: Comparison with previous works based on THz sensors.

Material	Analytes	LOD	Sensing type	IMG	[Reference]
MOSLS + MS (EIT)	**WP**	**6.25 ng/ml**	**Amplitude+ Frequency + Phase**	No π–π stacking	**This work**
MS (EIT)	MDK	0.5 ug/ml	Amplitude + frequency	No π–π stacking	[41]
Graphene + MS	Fructose	100 ng/ml	Amplitude	No π–π stacking	[42]
Graphene + PI	CMM	130 ng/ml	Amplitude	π–π stacking	[19]
Graphene + MS	CMM	20 ng/ml	Amplitude	π–π stacking	[42]

LOD, limit of detection; IMG, the interaction between external molecules and graphene; WP, whey protein. MS, metasurface; EIT, electromagnetically induced transparency; PI, polyimide; MDK, Midkine; CMM, chlorpyrifos methyl molecules.

The transmission T can be obtained through $T = 1 - g\chi_i$ [44], where g is the geometric parameter that indicates the coupling strength of the bright mode with the incident electric field E.

We defined two frequency bands, from 0.25 THz to 1 THz and from 0.62 THz to 1.58 THz, as two distinct regions of EIT-like effects. The measured transmission spectra of the PGPP@MS biosensor in these regions were

theoretically fitted with Eq. (2), as shown in Figure 3(b) and (c). The fitting results show reasonable consistency with the experiments.

The fitting parameters as a function of the CWP are shown in Figure 3(d) and (e) for the lower- and higher-frequency bands, respectively. It can be observed from Figure 3(d) that δ, κ, and γ_2 are almost constant in the low-frequency band, whereas γ_1 changes slightly with increasing CWP. The radiative damping of the bright mode resonator, γ_1, decreases to 4.1 THz at C_4, compared with 4.5 THz for a bare sensor.

In the high-frequency band (Figure 3(e)), δ is almost constant while γ_1, γ_2, and k change slightly with increasing CWP. The radiative damping of the bright mode resonator, γ_1, varies for CWP between C_2 and C_5. The non-radiative damping of the dark mode resonator, γ_2, changes from 3.8 THz at C_0 to 4.1 THz at C_5. At the same time, κ decreases from 5.2 to 5 THz^2 with increasing CWP. These variations in fitting parameters indicate that the physical properties of the analyte may affect the local field on the surface of the PGPP@MS biosensor, changing both the self- and mutual coupling of the bright and dark modes.

To characterize the sensing performance quantitatively, $\Delta V_T = V_{T0} - V_{Ti}$ (V_{T0} is transmission value at C_0, V_{Ti} is transmission value at C_i) and $\Delta f_n = |f_{ni} - f_{n0}|$ (f_{ni}/f_{n0} is for frequency resonances with and without protein) were calculated between the bare sample and each CWP from C_1 to C_5 at frequencies f_1–f_5. ΔV_T is shown in Figure 4(a), and Δf is shown in Figure 4(b).

With increasing CWP, the value of ΔV_T at f_1 is almost unchanged, ΔV_T at the f_2 peak increases slightly, and ΔV_T at f_3–f_5 increases significantly. ΔV_T reaches a maximum value of 0.4 at f_4 for a CWP of 316 μg/mL (C_4).

We selected the total transmission change at all frequency points, $\Delta V_{T\ total}$, for each CWP as the first biosensing index of the PGPP@MS platform. It is shown in Figure 4(d) (blue axis and markers). A significant change in $\Delta V_{T\ total}$ was observed with increasing CWP. When the concentration was 6.25 ng/mL (C_1), $\Delta V_{T\ total}$ was significantly different from the 0 to at C_0. $\Delta V_{T\ total}$ increases remarkably between concentrations C_1 and C_2 (2.52 μg/mL). When the concentration further increases to 316 μg/mL (C_4), $\Delta V_{T\ total}$ reaches about 82%.

The peaks and minima of the transmission spectrum also change with CWP. At the low end of the wave band, terahertz waves have low energy and are insensitive to environmental changes. Even at high CWP, almost no shift of f_1, f_2, or f_3 takes place (Figure 4(b)). However, when the

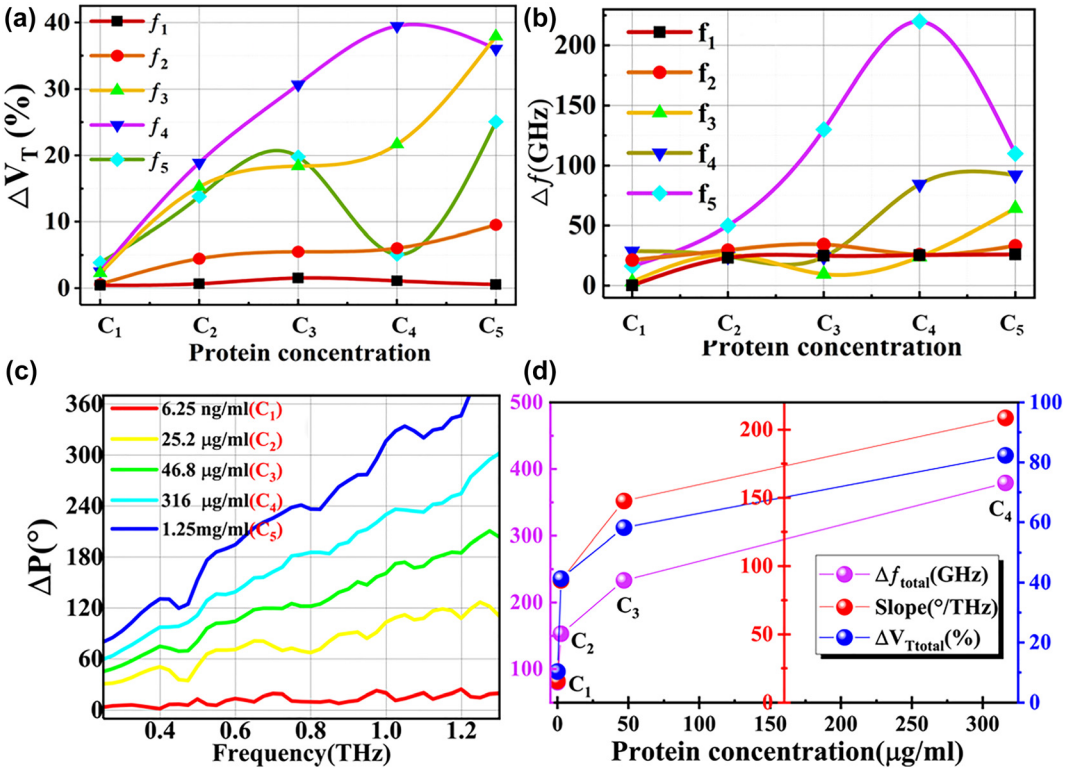

Figure 4: Quantitative analysis of multi-dimensional sensing performance.
(a) and (b) The transmission value difference ΔV_T (a) and frequency shift Δf (b) between the bare sensor and each CWP between C_1 and C_5 at frequencies f_1–f_5. (c) Phase difference ΔP between the bare sensor and each CWP tested. (d) Summary of the CWP dependence of the physical properties in (a)–(c). Blue axis and markers: The sum of transmission value difference ΔV_{Ttotal} for all frequency points. Purple axis and markers: total frequency shift Δf_{total}. Red axis and markers: fitted slopes of the phase difference, ΔP.

CWP is C_4, Δf_4 increases, then reaches a maximum value of 96 GHz at C_5. Δf_5 increases with increasing CWP to a maximum value of 224 GHz at C_4, then decreases.

The total frequency shift Δf_{total} of all frequency points is shown in Figure 4(d) (purple axes and markers) as the second biosensing index of the PGPP@MS platform. Δf_{total} increases with increasing CWP, reaching 350 GHz at 316 µg/mL whey protein (C_4). The result indicates that the PGPP@MS biosensor can detect frequency shifts as a useful sensing dimension.

The main sensing mechanism may be a change in the ultrasensitive photoconductivity properties of the MOSLS layer of the device based on the whey-protein-induced ED effect. This effect occurs when free electron/hole charges induced by electrostatic field excitations replace those normally supplied by a donor/acceptor dopant species. The distinct merit of ED is that the carrier concentration and polarity are tunable via external excitation.

Additionally, the phase change ΔP with and without whey protein was obtained for CWP ranging from C_1 to C_5, as shown in Figure 4(c). It is interesting to note that the dependence of phase difference on frequency is quasilinear. Consequently, the slope of the linear dependence can be considered a third biosensing index for PGPP@MS platforms. This is shown in Figure 4(d), where it can be seen that the change in slope is larger between lower concentrations. However, when the concentration grows from 46.8 µg/mL (C_3) to 316 µg/mL (C_4), the slope changes less rapidly. These results reveal that the phase is also altered after the introduction of protein, mainly because of the change in conductivity of perovskite. The maximum phase difference was 360° at 1.25 mg/mL (C_5) with a slope of ~400. Additionally, to verify this explanation, similar devices without perovskite were synthesized and the phase was measured under the same conditions. (See the Supplementary information for details.) The phase difference is almost zero as the CWP increases. Therefore, our claim that the phase change of the PGPP@MS biosensor is mainly caused by perovskite has been verified.

These results show that the PGPP@MS biosensor can function as a multidimensional biosensor capable of detecting ΔV_T, Δf and ΔP in the presence of proteins.

3.3 Physical rationale for the sensing mechanism

To provide a physical rationale for the PGPP@MS device's sensitivity, we propose a mechanism by which the ED effect [33] can be induced by protein molecules, illustrated in Figure 5. Without whey protein (Figure 5(a)), the energy band of perovskite is in its intrinsic state, and the initial Fermi level (E_{F0}) of the p-type graphene is in the valence band (Figure 5(c) and (e)) [45, 46]. Usually, protein aggregates have a positive net charge because amino acids exist in the form of ions in aqueous solution [47, 48]. When a positively charged protein is dropped onto the upper graphene surface as an analyte, its electrostatic field will cause charge accumulation in the graphene and perovskite layer (see Figure 5(b)). Consequently, the Fermi level shifts from E_{F0} to E_{F1} (compare Figure 5(c) and (d)), and the conductivity of graphene gradually increases, resulting in lower transmission, as in Figure 4(d). The electric field increases with CWP, increasing the strength of the ED response.

Simultaneously, the protein-induced ED effect may also cause changes in the conductivity of the perovskite layer by changing its charge polarity and carrier concentration; or in other words, by changing its Fermi level (see Figure 5(f)).

To understand the physical mechanism of the frequency shifts, we used modified perturbation theory to analyze the relationship between the Δf values and changes in the dielectric environment. The relative change in the angular frequency $\Delta\omega$ can be calculated by [11, 49–51]:

$$\frac{\Delta\omega_{AM}}{\omega_{AM}} = -\frac{1}{2}\frac{\int_0^h E_{AM}(r)\cdot(\epsilon-1)\cdot E_{AM}(r)\mathrm{d}r}{\int_0^\infty\left(|E_{AM}(r)|^2\right)\mathrm{d}r}, \tag{3}$$

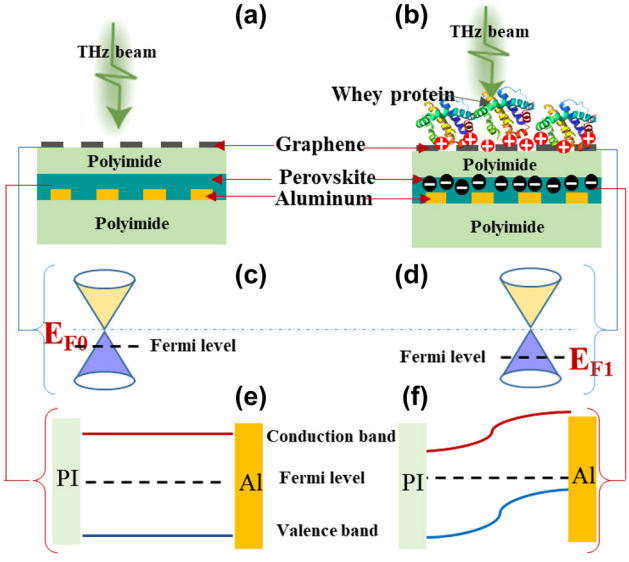

Figure 5: Schematic of the proposed sensing mechanism of the PGPP@MS biosensor.
(a) and (b) Schematic diagram of the balanced state and charge distribution in PGPP@MS without (a) and with (b) whey protein. (c) and (d) Schematic diagrams of the Fermi level of graphene for PGPP@MS without (c) and with (d) whey protein. (e) and (f) Energy band of the perovskite layer for PGPP@MS without (e) and with (f) whey protein.

where E_{AM} is the electric field in the original metasurface, and ε is the equivalent dielectric constant of PGPP@MS. Because the electric field decays exponentially along the direction normal to the metamaterial, the frequency shift calculated from Eq. (3) scales with the amount of analyte as follows:

$$\frac{\Delta\omega_{AM}}{\omega_{AM}} \propto \frac{(\epsilon - 1)\cdot h}{l} = \Delta\epsilon \cdot \frac{h}{l} \propto \Delta\epsilon, \tag{4}$$

where $\Delta\varepsilon$ is the difference in the equivalent dielectric constants with and without whey protein, h is the thickness of the monolayer of graphene (~1 nm), and L is the penetration depth of the THz field. It can be concluded that the conductivity of graphene and perovskite changes because of the incorporation of protein, leading to an alteration of the dielectric environment of the metasurface and an increase in Δf with increasing CWP. Both the mobility and concentration of charge carriers in graphene will reach a maximum and saturate even if the CWP increases further, hence why Δf_5 reached a maximum at C_4, then decreased.

3.4 Light-induced reversible sensing

Until now, reuse of, or reversible sensing by, THz metasurfaces biosensors has been seldom reported. However, by tuning the conductivity of the MOSLS with a laser, the transmission spectrum can in principle be restored to the state without protein. Our work provides an opportunity to achieve reversible sensing in the THz region. Because of the poor thermal stability of whey protein, laser illumination may degrade it, reducing the net charge and weakening the ED effect on the MOSLS.

To demonstrate reversible sensing, we measured the transmission value (V_T) of the biosensor at frequencies f_1–f_5 under illumination at wavelengths λ = 405 nm, 532 nm, and 808 nm and three different optical fluxes, $F_{op(1,\ 2,\ 3)}$. Pentagonal radar maps of the change in V_T are plotted in Figure 6. V_T is shown in gray for the bare sensor (C_0) and in red for the highest CWP tested, C_5, because it showed a clear response at all five frequencies (see Figure 4(a)). (The corresponding transmission spectra are shown in Figures S3–S5.) V_T after optical exposure is shown in yellow for 405 nm, green for 532 nm, or purple for 808 nm. As F_{op} increases (across rows in Figure 6), the optically induced V_T gradually increases from the initial value marked in red (corresponding to C_5) until it recovers to the value without protein, marked in gray.

At 405 nm and $F_{op(1)}$ = 1.1 mW/cm^2, only the V_T of f_5 increases. The main reason is that the laser power is too low to significantly influence the conductivity of the MOSLS. The V_T of all peaks increases for $F_{op(2)}$ = 11.5 mW/cm^2. At

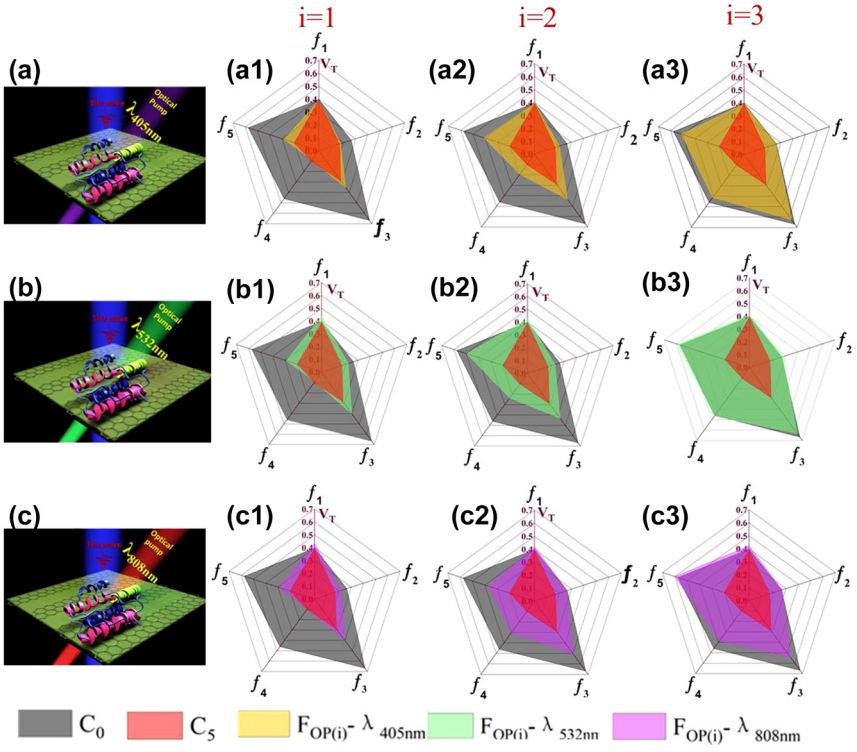

Figure 6: Description of reversible sensing. (a)–(c) Schematic diagrams of the PGPP@MS biosensor under THz beams and optical pumping at 405 nm (a), 532 nm (b), and 808 nm (c). (a1)–(a3) Pentagon radar maps of the transmission value (V_T) at frequency peaks f_1–f_5 under different optical fluxes, $F_{op(i)}$, at 405 nm. Every vertex in the radar maps represents V_T at a different frequency peak. Gray shapes represent V_T for the bare sensor, and red represents V_T when the protein concentration is C_5. V_T after 405 nm illumination is shown in yellow. i = 1: $F_{op(1)}$–$\lambda_{405\ nm}$ = 1.1 mW/cm^2. i = 2: $F_{op(2)}$–$\lambda_{405\ nm}$ = 11.5 mW/cm^2. i = 3: $F_{op(3)}$–$\lambda_{405\ nm}$ = 103.5 mW/cm^2. (b1)–(b3) Radar maps for V_T following 532 nm illumination (shown in green; other colors are as in (a)). i = 1: $F_{op(1)}$–$\lambda_{532\ nm}$ = 1.9 mW/cm^2. i = 2: $F_{op(2)}$–$\lambda_{532\ nm}$ = 42.4 mW/cm^2. i = 3: $F_{op(3)}$–$\lambda_{532\ nm}$ = 162.7 mW/cm^2. (c1)–(c3) Radar maps for V_T following 808 nm illumination (shown in purple; other colors are as in (a)). i = 1: $F_{op(1)}$–$\lambda_{808\ nm}$ = 2.2 mW/cm^2. i = 2: $F_{op(2)}$–λ_{808nm} = 28.3 mW/cm^2. i = 3: $F_{op(3)}$–$\lambda_{808\ nm}$ = 132.6 mW/cm^2.

$F_{op(3)} = 103.5\ mW/cm^2$, the transmission values of all peaks return almost completely to their original values. The V_T values behave similarly at 532 nm and 808 nm, indicating that protein-induced transmission changes are indeed reversible.

It is known that the absorption wavelength of perovskite is less than 780 nm, so while it may respond to light at 405 nm and 532 nm, it should not respond to illumination at 808 nm. However, the device shows responses to all three wavelengths, implying that graphene may be the main contributor to the conductivity of the MOSLS under optical excitation.

Theoretically, the conductivity of graphene (σ_{Gr}) is determined by the carrier densities, i.e., by the Fermi energy μ, and their effective temperature T [52]. Assuming that σ_{Gr} is a DC, low-signal-frequency conductivity determined by short-range scattering on defects and acoustic phonons, the scattering time $\tau = \tau_0\ (T_0/p\upsilon w) \propto 1/p$ [53], where τ_0 is the characteristic short-range scattering time [54]. Then one can obtain the following formula:

$$\sigma_{Gr} = \frac{2\sigma^0}{1 + e^{-\frac{\mu}{T}}}, \tag{5}$$

Where $\sigma^0 = e^2 T_0 \tau_0 / \pi h^2$ is the intrinsic conductivity under without any excitation conditions, $T = T_0$ and $\mu = 0$. At relatively weak irradiation, $|\mu| \ll T_0$, T, and Eq. (5) yields

$$\sigma_{Gr} \cong \sigma^0\left(1 + \frac{\mu}{2T}\right). \tag{6}$$

Laser excitation can drive electrons from the photo-excited electron-hole pairs to accumulate in the graphene layer, leading to a shift of the Fermi level from E_{F1} (Figure 5(d)) in the valence band toward the Dirac point caused by a reduction in μ. Meanwhile, the carriers inevitably cause a temperature increase. From Eq. (6), the conductivity of graphene decreases with enhanced optical pumping, and the transmission values of all the frequency peaks decrease. In summary, V_T increases after laser excitation, permitting reversible sensing.

4 Conclusions

We have designed, fabricated, and characterized a novel THz biosensor. It comprises a metal oxide semiconductor-like structure based on patterned graphene–polyimide–perovskite integrated with an EIT-like metasurface. Our PGPP@MS biosensor successfully detected whey protein concentrations as low as 6.25 ng/mL by detecting changes of frequency, amplitude, and phase, demonstrating multidimensional biosensing. Furthermore, ΔV_T, Δf, and ΔP increased significantly with whey protein concentration; $\Delta V_{T\ total}$, Δf_{total}, and ΔP approached 82%, 400 GHz, and 360° at 316 μg/mL whey protein, respectively. To explain the internal mechanism of ultra-sensitive, multi-dimensional biosensor performance, we carried out a theoretical analysis of the changes of the sensor's opto-electronic properties based on the ED effect. In addition, we have successfully realized reversible biosensing using lasers with several different wavelengths. This work could be of great importance for applications of THz meta-surfaces in the field of biosensing.

Acknowledgements: We thank Kaley McCluskey, PhD, from Edanz (www.liwenbianji.cn/) for editing a draft of this manuscript.

Author contribution: All the authors have accepted responsibility for the entire content of this submitted manuscript and approved submission.

Research funding: This work was supported by the National Natural Science Foundation of China (NSFC) (61701434, 61735010, 61675147), Special Funding of the Taishan Scholar Project (tsqn201909150), the Natural Science Foundation of Shandong Province (ZR2020FK008), the National Key Research and Development Program of China (2017YFB1401203, 2017YFA0700202), the Natural Science Foundation of Shandong Province (ZR2021MF014), funding from the Qingchuang Science and Technology Plan of Shandong Universities (2019KJN001).

Conflict of interest statement: The authors declare no conflicts of interest regarding this article.

References

[1] L. Wang, Y. Zhang, X. Guo et al., "A review of THz modulators with dynamic tunable metasurfaces," *Nanomaterials*, vol. 9, p. 965, 2019.

[2] M. Yang, T. Li, J. Gao et al., "Graphene–polyimide-integrated metasurface for ultrasensitive modulation of higher-order terahertz Fano resonances at the Dirac point," *Appl. Surf. Sci.*, vol. 562, p. 150182, 2021.

[3] M. Manjappa, Y. Srivastava, L. Cong, I. Al-Naib, and R. Singh, "Active photoswitching of sharp Fano resonances in THz metadevices," *Adv. Mater.*, vol. 29, p. 1603355, 2016.

[4] Y. K. Srivastava, A. Chaturvedi, M. Manjappa et al., "MoS_2 for ultrafast all-optical switching and modulation of THz Fano metaphotonic devices," *Adv. Opt. Mater.*, vol. 5, p. 1700762, 2017.

[5] H. Yao, X. Yan, M. Yang et al., "Frequency-dependent ultrasensitive terahertz dynamic modulation at the Dirac point on graphene-based metal and all-dielectric metamaterials," *Carbon*, vol. 184, pp. 400–408, 2021.

[6] N. I. Landy, S. Sajuyigbe, J. J. Mock, D. R. Smith, and W. J. Padilla, "Perfect metamaterial absorber," *Phys. Rev. Lett.*, vol. 100, p. 207402, 2008.
[7] J. Huang, J. Li, Y. Yang, J. Li, Y. Zhang, and J. Yao, "Active controllable dual broadband terahertz absorber based on hybrid metamaterials with vanadium dioxide," *Opt. Express*, vol. 28, pp. 7018–7027, 2020.
[8] A. Tittl, A. Leitis, M. Liu et al., "Imaging-based molecular barcoding with pixelated dielectric metasurfaces," *Science*, vol. 360, pp. 1105–1109, 2018.
[9] J. Zhang, N. Mu, L. Liu et al., "Highly sensitive detection of malignant glioma cells using metamaterial-inspired THz biosensor based on electromagnetically induced transparency," *Biosens. Bioelectron.*, vol. 185, p. 113241, 2021.
[10] W. Xu, L. Xie, J. Zhu et al., "Terahertz biosensing with a graphene-metamaterial heterostructure platform," *Carbon*, vol. 141, pp. 247–252, 2019.
[11] X. Yan, Z. Zhang, L. Liang et al., "A multiple mode integrated biosensor based on higher order Fano metamaterials," *Nanoscale*, vol. 12, pp. 1719–1727, 2020.
[12] Z. Zhang, M. Yang, X. Yan et al., "The antibody-free recognition of cancer cells using plasmonic biosensor platforms with the anisotropic resonant metasurfaces," *ACS Appl. Mater. Interfaces*, vol. 12, pp. 11388–11396, 2020.
[13] X. Yan, M. Yang, Z. Zhang et al., "The terahertz electromagnetically induced transparency-like metamaterials for sensitive biosensors in the detection of cancer cells," *Biosens. Bioelectron.*, vol. 126, pp. 485–492, 2019.
[14] M. Yang, L. Liang, Z. Zhang et al., "Electromagnetically induced transparency-like metamaterials for detection of lung cancer cells," *Opt. Express*, vol. 27, pp. 19520–19529, 2019.
[15] K. A. Niessen, M. Xu, D. K. George et al., "Protein and RNA dynamical fingerprinting," *Nat. Commun.*, vol. 10, pp. 1–10, 2019.
[16] C. H. Lu, H. H. Yang, C. L. Zhu, X. Chen, and G. N. Chen, "A graphene platform for sensing biomolecules," *Angew. Chem.*, vol. 48, pp. 4785–4787, 2009.
[17] M. Nagel, M. Först, and H. Kurz, "THz biosensing devices: fundamentals and technology," *J. Phys. Condens. Matter*, vol. 18, pp. S601–S618, 2006.
[18] R. Wang, W. Xu, D. Chen et al., "Ultrahigh-sensitivity molecular sensing with carbon nanotube terahertz metamaterials," *ACS Appl. Mater. Interfaces*, vol. 12, pp. 40629–40634, 2020.
[19] W. Xu, Y. Huang, R. Zhou et al., "Metamaterial-free flexible graphene-enabled terahertz sensors for pesticide detection at bio-interface," *ACS Appl. Mater. Interfaces*, vol. 12, pp. 44281–44287, 2020.
[20] T. C. Tan, Y. K. Srivastava, R. T. Ako et al., "Active control of nanodielectric-induced THz quasi-BIC in flexible metasurfaces: a platform for modulation and sensing," *Adv. Mater.*, vol. 33, p. 2100836, 2021.
[21] D. Rodrigo, O. Limaj, D. Janner et al., "Mid-infrared plasmonic biosensing with graphene," *Science*, vol. 349, pp. 165–168, 2015.
[22] A. Nag, A. Mitra, and S. C. Mukhopadhyay, "Graphene and its sensor-based applications: a review," *Sens. Actuator A Phys.*, vol. 270, pp. 177–194, 2018.
[23] N. S. Green and M. L. Norton, "Interactions of DNA with graphene and sensing applications of graphene field-effect transistor devices: a review," *Anal. Chim. Acta*, vol. 853, pp. 127–142, 2015.
[24] J. Feng, W. Li, X. Qian, J. Qi, L. Qi, and J. Li, "Patterning of graphene," *Nanoscale*, vol. 4, pp. 4883–4899, 2012.
[25] S. Shukla, S.-Y. Kang, and S. J. A. P. R. Saxena, "Synthesis and patterning of graphene: strategies and prospects," *Appl. Phys. Rev.*, vol. 6, p. 021311, 2019.
[26] A. Dimiev, D. V. Kosynkin, A. Sinitskii, A. Slesarev, Z. Sun, and J. M. Tour, "Layer-by-layer removal of graphene for device patterning," *Science*, vol. 331, pp. 1168–1172, 2011.
[27] H. Jung, H. Jo, W. Lee et al., "Electrical control of electromagnetically induced transparency by terahertz metamaterial funneling," *Adv. Opt. Mater.*, vol. 7, p. 1801205, 2019.
[28] R. Wang, M. Mujahid, Y. Duan, Z. K. Wang, J. Xue, and Y. Yang, "A review of perovskites solar cell stability," *Adv. Funct. Mater.* vol. 29, p. 1808843, 2019.
[29] J. P. Attfield, P. Lightfoot, and R. E. Morris, "Perovskites," *Dalton Trans.*, vol. 44, pp. 10541–10542, 2015.
[30] S. D. Stranks and H. J. Snaith, "Metal-halide perovskites for photovoltaic and light-emitting devices," *Nat. Nanotechnol.*, vol. 10, pp. 391–402, 2015.
[31] Z. Hailiang, Z. Minxuan, and H. Yue, "Performance optimization of conventional MOS-like carbon nanotube FETs with realistic contacts based on stair-case doping strategy," *Solid State Electron.*, vol. 54, pp. 1572–1577, 2010.
[32] J. A. L. López, J. C. López, M. Aceves-Mijares et al., "Photoelectric properties of MOS-like structures with twofold SRO films," *Procedia Eng.*, vol. 25, pp. 329–333, 2011.
[33] G. Gupta, B. Rajasekharan, and R. J. E. Hueting, "Electrostatic doping in semiconductor devices," *IEEE Trans. Electron. Dev.*, vol. 64, pp. 3044–3055, 2017.
[34] A. Vaysset, S. Martinie, F. Triozon et al., "MOS-like approach for compact modeling of high-electron-mobility transistor," *2020 International Conf. on Simulation of Semiconductor Processes and Devices (SISPAD)*, IEEE, 2020, pp. 221–224.
[35] G. Xu, Y. Zhang, X. Duan, A. A. Balandin, and K. L. Wang, "Variability effects in graphene: challenges and opportunities for device engineering and applications," *Proc. IEEE*, vol. 101, pp. 1670–1688, 2013.
[36] C. L. Davies, J. B. Patel, C. Q. Xia, L. M. Herz, and M. B. Johnston, "Temperature-dependent refractive index of quartz at terahertz frequencies," *J. Infrared, Millim. Terahertz Waves*, vol. 39, pp. 1236–1248, 2018.
[37] S. H. Abedinpour, G. Vignale, A. Principi, M. Polini, W. K. Tse, and A. H. MacDonald, "Drude weight, plasmon dispersion, and ac conductivity in doped graphene sheets," *Phys. Rev. B*, vol. 84, 2011, Art no. 045429.
[38] G. Jnawali, Y. Rao, H. Yan, and T. F. Heinz, "Observation of a transient decrease in terahertz conductivity of single-layer graphene induced by ultrafast optical excitation," *Nano Lett.*, vol. 13, pp. 524–530, 2013.
[39] Y. Cheng, K. Zhang, Y. Liu, S. Li, and W. Kong, "Actively mode tunable electromagnetically induced transparency in a polarization-dependent terahertz metamaterial," *AIP Adv.*, vol. 10, p. 045026, 2020.
[40] K. Zhang, Y. Liu, H. Wu, F. Xia, and W. Kong, "Dynamically selective control of dual-mode electromagnetically induced transparency in terahertz metal-graphene metamaterial," *OSA Continuum*, vol. 3, pp. 505–514, 2020.
[41] X. Guo, Z. Zhang, M. Yang et al., "Time-frequency double domain resolving by electromagnetically induced transparency

metasensors for rapid and label-free detection of cancer biomarker midkine," *Opt. Laser. Eng.*, vol. 142, p. 106566, 2021.
[42] R. Zhou, C. Wang, Y. Huang et al., "Label-free terahertz microfluidic biosensor for sensitive DNA detection using graphene-metasurface hybrid structures," *Biosens. Bioelectron.*, vol. 188, p. 113336, 2021.
[43] S. Xiao, T. Wang, T. Liu, X. Yan, Z. Li, and C. Xu, "Active modulation of electromagnetically induced transparency analogue in terahertz hybrid metal-graphene metamaterials," *Carbon*, vol. 126, pp. 271–278, 2018.
[44] J. Ding, B. Arigong, H. Ren et al., "Tuneable complementary metamaterial structures based on graphene for single and multiple transparency windows," *Sci. Rep.*, vol. 4, p. 6128, 2014.
[45] S. Winnerl, M. Orlita, P. Plochocka et al., "Carrier relaxation in epitaxial graphene photoexcited near the Dirac point," *Phys. Rev. Lett.*, vol. 107, p. 237401, 2011.
[46] M. Ryzhii, V. Ryzhii, T. Otsuji et al., "Double injection, resonant-tunneling recombination, and current-voltage characteristics in double-graphene-layer structures," *J. Appl. Phys.*, vol. 115, p. 024506, 2014.
[47] A. Kharlamova, C. Chassenieux, and T. Nicolai, "Acid-induced gelation of whey protein aggregates: kinetics, gel structure and rheological properties," *Food Hydrocolloids*, vol. 81, pp. 263–272, 2018.
[48] K. N. Ryan, Q. Zhong, and E. A. Foegeding, "Use of whey protein soluble aggregates for thermal stability – a hypothesis paper," *J. Food Sci.*, vol. 78, pp. R1105–R1115, 2013.
[49] X. Wu, B. Quan, X. Pan et al., "Alkanethiol-functionalized terahertz metamaterial as label-free, highly-sensitive and specificbiosensor," *Biosens. Bioelectron.*, vol. 42, pp. 626–631, 2013.
[50] S. M. Hanham, C. Watts, W. J. Otter, S. Lucyszyn, and N. Klein, "Dielectric measurements of nanoliter liquids with a photonic crystal resonator at terahertz frequencies," *Appl. Phys. Lett.*, vol. 107, p. 032903, 2015.
[51] C. Wu, A. B. Khanikaev, R. Adato et al., "Fano-resonant asymmetric metamaterials for ultrasensitive spectroscopy and identification of molecular monolayers," *Nat. Mater.*, vol. 11, pp. 69–75, 2012.
[52] V. Ryzhii, M. Ryzhii, T. Otsuji, V. Leiman, V. Mitin, and M. Shur, "Modulation characteristics of uncooled graphene photodetectors," *J. Appl. Phys.*, vol. 129, p. 214503, 2021.
[53] A. Satou, F. Vasko, and V. Ryzhii, "Nonequilibrium carriers in intrinsic graphene under interband photoexcitation," *Phys. Rev. B*, vol. 78, p. 115431, 2008.
[54] V. Ryzhii, A. A. Dubinov, T. Otsuji, V. Mitin, and M. S. Shur, "Terahertz lasers based on optically pumped multiple graphene structures with slot-line and dielectric waveguides," *J. Appl. Phys.*, vol. 107, p. 054505, 2010.

Supplementary Material: The online version of this article offers supplementary material (https://doi.org/10.1515/nanoph-2021-0816).